NANO LETTERS

pubs.acs.org/NanoLett

Letter

Quantum-Dot Single-Electron Transistors as Thermoelectric Quantum Detectors at Terahertz Frequencies

Mahdi Asgari, Dominique Coquillat, Guido Menichetti, Valentina Zannier, Nina Diakonova, Wojciech Knap, Lucia Sorba, Leonardo Viti,* and Miriam Serena Vitiello*

Cite This: *Nano Lett.* 2021, 21, 8587−8594

Read Online

ACCESS | Metrics & More | Article Recommendations | Supporting Information

ABSTRACT: Low-dimensional nanosystems are promising candidates for manipulating, controlling, and capturing photons with large sensitivities and low noise. If quantum engineered to tailor the energy of the localized electrons across the desired frequency range, they can allow devising of efficient quantum sensors across any frequency domain. Here, we exploit the rich few-electron physics to develop millimeter-wave nanodetectors employing as a sensing element an InAs/$InAs_{0.3}P_{0.7}$ quantum-dot nanowire, embedded in a single-electron transistor. Once irradiated with light, the deeply localized quantum element exhibits an extra electromotive force driven by the photothermoelectric effect, which is exploited to efficiently sense radiation at 0.6 THz with a noise equivalent power <8 $pWHz^{-1/2}$ and almost zero dark current. The achieved results open intriguing perspectives for quantum key distributions, quantum communications, and quantum cryptography at terahertz frequencies.

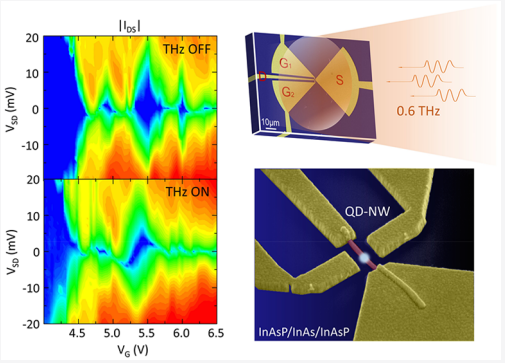

KEYWORDS: *quantum dots, quantum detectors, terahertz, quantum engineering*

Applications in quantum information technology usually require a tight control of the orbital states of a single electron, needed to encode and transfer information with high fidelity.[1] This has recently stimulated a wide interest in efficient, low-noise receivers that can detect a controlled photon number (photon counters) or even single photons,[2] the ultimate limit of detection sensitivity, in quantum nanostructures. This has long been inaccessible for terahertz (THz) or gigahertz waves (wavelengths in the range from 60 μm to 1 mm) because of the small energy quanta, as small as a part per 1000 of the photon energies in the visible or near-infrared regions. However, the far-infrared region of the electromagnetic spectrum discloses a peculiar potential in this respect: it is a rich domain of spectroscopy and metrological research and a frontier region for a variety of applications in biomedical diagnostics,[3] quality and process controls,[4] security,[5] high-data-rate wireless communication,[6] optical quantum cryptography,[7] and quantum key distribution.[8]

Quantum detectors, conventionally employed in the visible, near-infrared, or mid-infrared regimes, including photodiodes,[9] photoconductors,[10] phototransistors,[11] charge-coupled detectors (CCDs),[12] photomultiplier tubes,[13] or semiconductor quantum-well infrared photodetectors (QWIPs),[14] are devices that convert incoming photons directly into an electrical signal, as opposed to thermal detectors that rely on the conversion of incoming radiation to heat.[15] QWIPs represent the benchmark technology for quantum applications in the mid-infrared frequency range,[16] owing to the high sensitivity and ultrafast response times and the short lifetime of the intersubband transitions (τ_{IST} ∼ picoseconds).[15] Moreover, intersubband transitions in quantum wells (QWs) go along with pronounced optical nonlinearities, resulting in huge nonlinear coefficients for second harmonic generation, more than 3 orders of magnitude larger than those of the host GaAs material.[17] Pushing the operation of QWIPs in the far-infrared is, however, extremely challenging as a result of the low energy of far-infrared photons. Only a few reports at high terahertz frequencies (4.5−7.0 THz) are presently available in either a standard mesa configuration, normally substrate-coupled through a polished facet,[16] a double-metal patch-antenna array architecture,[18] or a metamaterial configuration with dimensions below the diffraction limit,[19] at 3 THz, and with a maximum speed of 3 GHz in an array configuration.[20]

Quantum-dot infrared photodetectors (QDIPs) represent a promising route to overcome some of the major limitations of terahertz QWIPs.[21] In particular, the energy level configuration and the orbital occupation can be controlled via the QD diameter−height and the gate bias, respectively. QDs are also inherently sensitive to normal incidence photoexcitation and,

Received: May 31, 2021
Revised: July 27, 2021
Published: October 7, 2021

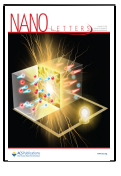

https://doi.org/10.1021/acs.nanolett.1c02022
Nano Lett. 2021, 21, 8587−8594

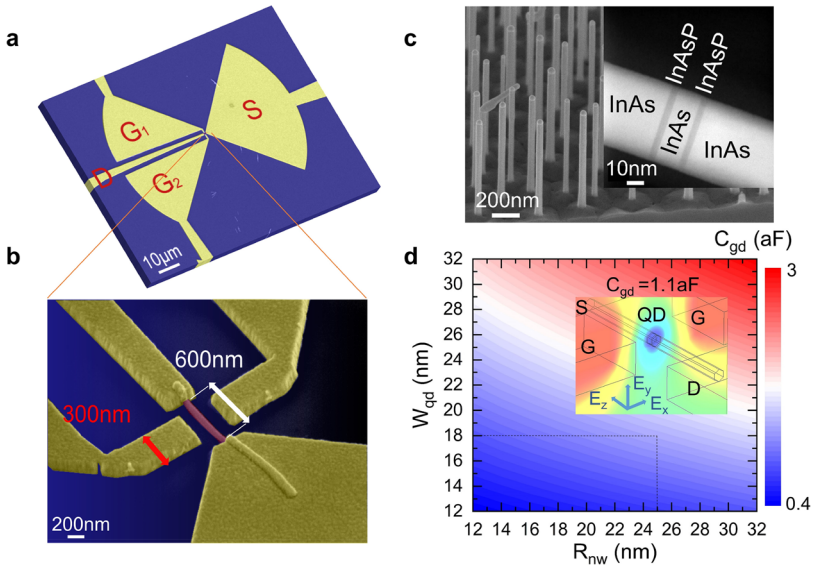

Figure 1. (a) Scanning electron microscopy (SEM) image of a planar on-chip split bow-tie antenna. One side of the antenna is connected to the source electrode, while the opposite side is connected to the arms of double lateral gate contacts. (b) SEM image of a prototypical quantum-dot nanowire (QD−NW) single-electron transistor (SET). (c) SEM image of a forest of epitaxially grown InAs nanowires. (Inset) Scanning transmission electron microscopy (STEM) image of a single InAs/InAsP QD−NW. (d) Color map of the gate−QD capacitance (C_{gd}) as a function of the QD axial dimension (distance between the barriers, W_{qd}) and NW radius (R_{nw}), calculated numerically using an electrostatic simulation of the QD−NW FET performed with commercial software (COMSOL Multiphysics). (Inset) Three-dimensional image of the SET channel overlaid to the simulated distribution of electrostatic potential around the InAs QD. The simulated C_{gd} value is 1.1 aF for our specific device geometry (W_{qd} = 18 nm and R_{nw} = 25 nm).

therefore, do not require 45° polished facets, metal gratings,[22] engineered band mixing,[22,23] or reflectors, as conventionally needed for QWIPs.[23] Owing to the discrete density of states, they are well-suited for tunable narrow band detection. Most importantly, the three-dimensional confinement leads to the phonon bottleneck effect,[24] inhibiting phonon scattering in QDs compared to QWs[23,25] and increasing the lifetime of photoexcited carriers (∼5−10 ps),[23] whose phonon-mediated relaxation to the ground state is eventually hindered in favor of an enhanced probability of tunneling out of the dot. This effect is then expected to give rise to a more efficient detection, as a consequence of a larger quantum efficiency and to enable operation at higher temperatures (up to 50−60 K).[21,23] The reduced dependence of the density of states upon the temperature and the longer carrier lifetime (1−2 orders of magnitude) in QDs have the additional advantage of reducing the dark current with respect to QWIPs.[26]

QDIPs are promising candidates for applications in terahertz communication.[15,27,28] Once implemented in a single-electron transistor (SET) geometry, a low noise equivalent power (NEP) of $\sim 10^{-19}$ $WHz^{-1/2}$[15,28] can be indeed engineered under a precise control of bias.[15] When illuminated with a radiation energy that is not in resonance with the QD intersubband transition, QD-based devices still exhibit good detection performances (e.g., responsivity up to 100 A/W[29]), owing to the inherently strong nonlinearity of the current−voltage characteristics.

Here, we conceive and devise QD millimeter-wave nanodetectors employing InAs/InAsP QD nanowires (NWs) that, thanks to the small effective mass and favorable Fermi level pinning,[30,31] give rise to localized QDs characterized by large charging energy.[31,32] Employing the confinement defined by the double-barrier heterostructure, we engineer a QD SET that, once irradiated with light, exhibits an extra electromotive force driven by the photothermoelectric (PTE) effect, which can be exploited to efficiently sense the incoming radiation with NEP levels down to 8 $pWHz^{-1/2}$. Importantly, the demonstrated PTE quantum detectors operate under zero bias; therefore, the dark current is largely reduced with respect to standard configurations employing biased systems.[16,18,19]

In the last years, heterostructured semiconductor NWs proved to be a promising technological platform[33] for devising sensitive, high-speed, low-noise detectors across the terahertz.[34] NW field effect transistors (FETs) with controlled and tailored composition[26] are compatible with on-chip technologies[33] and are featured with a characteristic attofarad-order capacitance that makes them well-suited for low-capacitance integrated circuits.[35,36] Even though the stoichiometric and geometric control in the growth of axially heterostructured NWs can allow for tailoring tunnel barrier properties on purpose, it does not allow for a widely tunable tunnel coupling compared to electrostatically defined structures.[37] This provides an important benefit for efficient thermoelectric conversion[31,38] or for single-photon QD detectors, which may require a broadly different range of tunneling rates.[39] An alternative, more efficient strategy to simultaneously optimize charge stability and tunneling relies on engineering and tuning electrostatically the orbital configuration within the QD.[40]

We here exploit InAs/$InAs_{0.3}P_{0.7}$ QD−NWs grown via a gold-assisted chemical beam epitaxy (CBE). This material system allows for combining semiconductors with different lattice parameters in axial heterostructures thanks to the efficient strain relaxation along the NW sidewalls. Moreover, the InAs/InP system is particularly suitable for the realization of high-quality axial NW heterostructures like QDs and superlattices in Au-assisted growth. Indeed, the very low solubility of both As and P into Au allows for the acquisition of atomically sharp interfaces in both growth directions.[41] However, in the case of NWs grown from a metal seed nanoparticle (NP) by the vapor−liquid−solid (VLS) mecha-

https://doi.org/10.1021/acs.nanolett.1c02022
Nano Lett. 2021, 21, 8587−8594

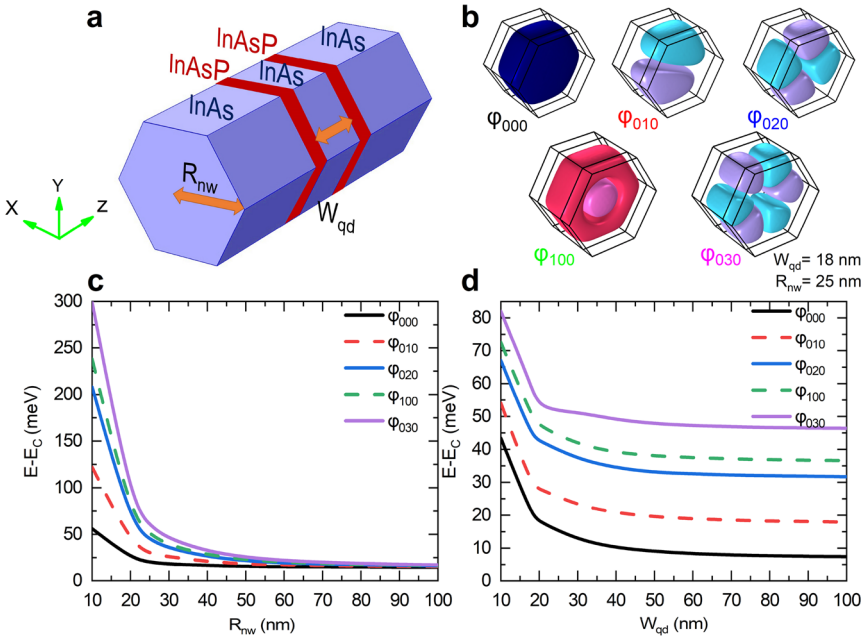

Figure 2. (a) Three-dimensional hexagonal wurtzite structure of the axially grown QD−NW, employed in our numerical simulations. (b) Distribution of the electron wave function (orbital configuration) for the first five energy states of a QD having the following dimensions: NW radius (R_{nw} = 25 nm) and QD width along the growth direction (W_{qd} = 18 nm). (c and d) Energy of the electronic states localized in the QD, plotted as a function of R_{nw} and W_{qd} of the QD, respectively. Color lines (marked with letters, corresponding to panel b) present the evolution of the orbital energies. The ground state (black line) energy is E_{000} > 55 meV when R_{nw} approaches 10 nm and decreases noticeably while increasing the radius up to 50 nm (E_{000} < 20 meV). As expected, the confinement also depends upon W_{qd}. The energies of the radially confined states (quantum number g = 0, panel b) as a function of W_{qd}. Interestingly, while the energy spacing between g = 0 levels steadily decreases with R_{nw} (c), it remains almost unaltered when W_{qd} increases from 40 to 100 nm (d), demonstrating the strong correlation of quantum confinement to the geometrical characteristics.

nism, the chemical composition of the NP changes when the growth is switched from one material to the other, and this strongly affects the NP stability, the growth mode (straight or kinked), and the growth rate.[41,42] In particular, the growth of alternating InAs/InP segments is prone to nucleation delay during the growth of the InP segment that can lead to NP reconfiguration, which, in turn, affects the growth dynamics.[42] On the other hand, if $InAs_{(1-x)}P_x$ alloys instead of InP are grown on top of InAs NWs, the nucleation delay is not present. As a consequence, the growth of InAs/$InAs_{(1-x)}P_x$ heterostructures is uniform and very symmetric thicknesses are obtained for the same growth times. Finally, the height of the tunneling barriers can be tuned by changing the P/As ratio in the alloy segments.[43]

A 18 nm long segment of InAs with band gap E_g = 0.40 eV and electron effective mass m^* = 0.063m_e,[44] where m_e is the free electron mass, is confined by thin (5 ± 2 nm) $InAs_{0.3}P_{0.7}$ barriers with relatively high E_g = 1.03 eV and m^* = 0.067m_e,[45] leading to quantum confinement along the NW axial direction. The resulting InAs/$InAs_{0.3}P_{0.7}$ QD−NWs are transferred from the growth substrate over a 300 nm/350 μm SiO_2/intrinsic silicon wafer, where the detectors are nanofabricated. Individual NWs are integrated in planar laterally gated FETs[46] (panels a−c of Figure 1), employing a combination of electron beam lithography (EBL) and thermal evaporation (see the Supporting Information). Under this configuration, the nanosystem behaves like a few-electron transistor and the electrical transport can be described within the framework of the constant interaction model.[47] The self-capacitance of the QD (C_Σ) defines the charging energy $\delta = e^2/C_\Sigma$ required for adding one electron to the dot. Together with the capacitance between the QD and the gate electrode (C_{gd}; Figure 1d), it determines the gate lever arm, $\alpha_G = C_{gd}/C_\Sigma$, which is explicitly related to the capacitive coupling with the gate electrode. If $\delta \geq k_B T$, with k_B being the Boltzmann constant and T being the temperature, the source (S) to drain (D) current is expected to exhibit a set of sharp peaks as a function of the gate voltage (V_G), corresponding to the resonant tunneling of single electrons through the QD and reflecting Coulomb interactions between electrons.[46] In this Coulomb blockade regime,[48] the voltage interval between consecutive peaks is defined by the sum of the energy level spacing ΔE and the charging energy.[48] By properly choosing the geometrical parameters of the dot, i.e., NW radius (R_{nw}) and width of the InAs segment (Figure 1c) between the two $InAs_{0.3}P_{0.7}$ barriers (W_{qd}), the distance between consecutive energy levels can be tailored to be resonant with a desired photon energy.

To couple the QD−NW-based FET to the 0.6 THz field, the deeply sub-wavelength QD element is asymmetrically integrated in a planar bow-tie antenna,[33] with radius 210 μm (Figure 1a). The asymmetry is ensured by the connection of the antenna arms to the S and lateral gate (G) electrodes.

We compute the eigenstates $|\varphi_{nlg}\rangle$ and eigenenergies φ_{nlg} of axially grown QDs by iteratively solving the coupled Schrödinger−Poisson equations; here, the quantum numbers n, l, and g distinguish between levels confined along the radial, angular, and growth directions, respectively. The QD model is geometrically sketched in Figure 2a, and the simulation results are shown in panels b−d of Figure 2. The computed energy spacing between the ground level and the first excited state is ~9 meV for our specific QD geometry.

https://doi.org/10.1021/acs.nanolett.1c02022
Nano Lett. 2021, 21, 8587−8594

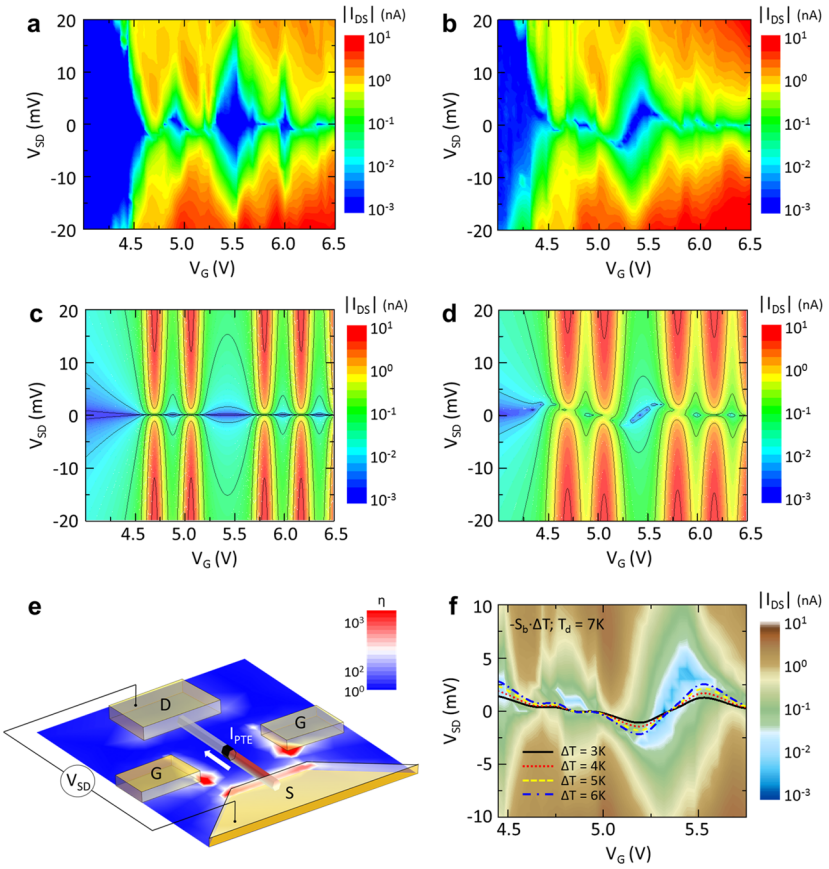

Figure 3. Low-temperature electrical transport through the single-electron transistor in the dark (a and c) and illuminated (b and d) states. The absolute drain-source current $|I_{DS}|$ is plotted as a function of V_{SD} (vertical axis) and V_G (horizontal axis) in a logarithmic scale. (a) Experimental dark state showing a typical Coulomb charge stability diagram, where the characteristic diamonds corresponding to a fixed electron population N = 1, 2, and 3 are resolved. (b) $|I_{DS}|$ map measured when the 0.6 THz radiation is illuminating the device, showing smeared and tilted Coulomb diamonds. (c and d) Theoretical charge stability diagrams. (c) Calculated terahertz-off map with the thermoelectric model, assuming that the dot temperature T_d is equal to the heat-sink temperature $T_d = T_0 = 4$ K. (d) Calculated evolution of the Coulomb blockade diagram under illumination: a longitudinal source-drain thermal gradient $\Delta T = 5$ K and a global heating of the dot $T_d = 7$ K are assumed. (e) Schematic diagram of the detection mechanism: the sign of the photothermoelectric (PTE) contribution to the current is determined by the direction of the thermal gradient and the sign of the Seebeck coefficient of the QD. The background color map is a numerical simulation of the electromagnetic energy density enhancement (η) under terahertz illumination. (f) Overlay between the experimental $|I_{DS}|$ color map and the PTE electromotive force $V_{PTE} = -S_b\Delta T$, calculated assuming different terahertz-induced ΔT = 3, 4, 5, and 6 K and $T_d = 7$ K.

We investigate the electron transport through the SET by measuring the charge stability diagram at a heat-sink temperature $T_0 = 4.2$ K. The detector is mounted in a pulse-tube optical cryostat with helium exchange gas (Janis Research), and the source-drain current (I_{SD}) is recorded as a function of both the source-drain bias (V_{SD}) and the gate voltage (V_G). The Coulomb blockade diagram (Figure 3a) shows diamonds corresponding to regions where the conductance is suppressed, because single-electron tunneling processes are not allowed and the electron occupation (N) in the QD is fixed. By spanning V_G beyond the pinch-off voltage ($V_G = 4.5$ V), if both the thermal energy (k_BT) and the source-drain biasing energy (eV_{SD}) are smaller than the charging energy of the QD ($k_BT \leq eV_{SD} \leq e^2/C_\Sigma$), a set of conduction peaks are visible as a result of the progressive alignment of electrochemical potential on the S and D sides with the QD energy levels. Between two consecutive peaks, resonant tunneling through the barriers is inhibited and the charge stability condition is satisfied. Importantly, the transport characteristics of the SET in the Coulomb blockade regime, being related to the single-particle energy states and their mutual interactions, allow for describing the electronic features of the device. In particular, employing the constant interaction model,[47] we evaluate the capacitive coupling between the QD and the gate electrode (C_{gd}), the charging energy, and the energy level spectrum (see the Supporting Information). We extract from Figure 3a: $e^2/C_\Sigma = 6.9$ meV, an energy level spacing $\Delta E = 7.0$ meV (in reasonable agreement with the value obtained by our Schrödinger–Poisson model), $C_\Sigma = 55$ aF, $C_{gd} = 1.1$ aF, and $\alpha_G = C_{gd}/C_\Sigma = 18.8$ mV/V.

Once funneling the terahertz beam onto the detection element (see the Supporting Information), the retrieved direct current map appears visibly altered (Figure 3b). The clearest features are the distorted Coulomb diamonds and the shift of the current peaks toward larger V_G compared to the corresponding peaks measured without terahertz radiation (Figure 3a). In particular, the current vanishes to zero at different V_{SD} and different V_G, very differently from what happens in the dark (Figure 3a), where, for any given V_G, it approaches zero at $V_{SD} = 0$ V.

We ascribe this behavior to the photothermoelectric effect, generated by the thermal gradient (ΔT) between the left and right side of the QD–NW: the bow-tie antenna funnels the radiation asymmetrically, producing a field enhancement, that

https://doi.org/10.1021/acs.nanolett.1c02022
Nano Lett. 2021, 21, 8587–8594

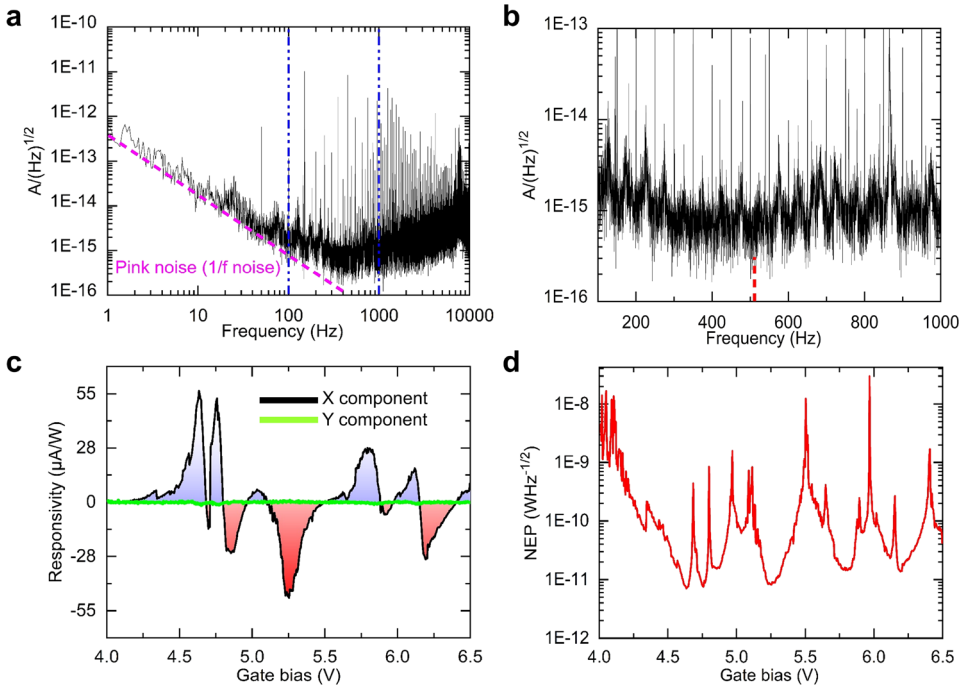

Figure 4. (a) Noise spectral density (NSD) as a function of frequency measured by a spectrum analyzer. The pink dashed line is referring to the predicted $1/f$ noise contributor. The dotted blue lines mark the region of low noise. (b) Zoom of the NSD of panel (a) plotted in the range from 100 Hz to 1 kHz, while the red dashed line refers to the frequency equal to 518 Hz. (c) Responsivity measured under illumination at 0.6 THz, at low temperature (T = 4.2 K), plotted as a function of V_G while keeping V_{SD} fixed at zero and measuring the x and y components of the lock-in amplifier. (d) Noise equivalent power (NEP) plotted as a function of V_G.

is mainly confined between the S and G electrodes, leaving the drain side colder with respect to the source side of the QD.

Figure 3e schematically displays the detection mechanism, overlaid to the numerically simulated (finite element method, COMSOL Multiphysics) electromagnetic energy enhancement (η) induced by the terahertz beam at the source side of the NW. In this picture, the total current flowing along the SET channel is $I_{DS} = \sigma_0(V_{SD} + S_b\Delta T)$, where $\sigma_0 = dI_{SD}/dV_{SD}$ is the electronic conductance and S_b represents the QD Seebeck coefficient (or thermopower). Under illumination, the distortion of the Coulomb diamonds is given by the additional electromotive force $V_{PTE} = S_b\Delta T$, which is identified in the current map (Figure 3b) by the V_{SD} values at which the current vanishes along the gate voltage sweep (it takes a finite V_{SD} to counterbalance V_{PTE}). Therefore, the amplitude and sign of V_{PTE} are ultimately determined by the QD thermopower S_b. It is worth noticing that, by taking advantage of the PTE mechanism, our scheme allows for zero-bias, zero-dark current operation, limiting the detector noise to intrinsic charge or temperature fluctuations.

Such a qualitative interpretation of the PTE detection is then supported by the quantitative comparison of the experimental data to the outcome of a numerical model of charge and heat transport through the QD based on the Landauer approach[49,50] to evaluate its thermoelectric properties, starting from electrical parameters that mimic our experimental configuration (see the Supporting Information). The results, shown in Figure 3c, exhibit a good agreement with the experimental data (Figure 3a). When the terahertz beam is illuminating the detector, we expect that a thermal gradient ΔT between the left (S) and right (D) leads of the QD is established, as a consequence of the asymmetric coupling provided by the bow-tie antenna (Figure 3e). In addition to ΔT, the evaluation of the theoretical map for the illuminated case (Figure 3d) also considers a global heating of the dot ($T_d > T_0$, where T_d is the dot temperature). This accounts for the fact that the QD, being approximately located at the center of the SET, will reach, at steady state, an intermediate temperature between those of the S and D extremes. By comparing the model to the experimental results, we estimate an overall increase of T_d from 4 K (T_0) in the dark state to 7 K in the illuminated case, with a terahertz-induced temperature difference ΔT = 5 K between the leads. The increase of T_d has the effect of increasing the Coulomb peak broadenings (see the Supporting Information), whereas ΔT gives rise to a clear Seebeck effect, which corresponds to the additional electromotive force ($-S_b\Delta T$) acting on the dot. Such a picture is nicely captured by the superposition of the $|I_{DS}|$ map in the illuminated case (terahertz on) with the theoretical contour lines corresponding to $I_{DS} = 0$ ($V_{SD} = -S_b\Delta T$), calculated for different values of ΔT (Figure 3f).

We ascribe the small discrepancy between the proposed model and the experimental results to the possible contribution of the photogating effect[51] and to the gate voltage and temperature-dependent conductivity of the InAs NW segments on the left and right side of the dot, which are not taken into account. However, the developed simplified thermoelectric model clearly highlights the main thermal effects governing the photodetection process.

We finally extrapolate the gate bias-dependent detector responsivity (R_a) to evaluate the main figures of merit of the devised QD NW photodetector (see the Supporting Information). As shown in Figure 4c, the observed dependence of R_a from V_G is correlated with the sharp transport peaks retrieved via transport experiments (Figure 3b). In particular, the multiple sign changes of the photoresponse reflect the sign

https://doi.org/10.1021/acs.nanolett.1c02022
Nano Lett. 2021, 21, 8587−8594

changes of the thermopower S_b around each Coulomb peak, and R_a reaches a maximum value of 55 μA/W. The corresponding noise equivalent power (NEP)[52] is determined by the ratio between the noise spectral density (NSD) and R_a. The NSD is measured by connecting D to a Dacron dynamic spectrum analyzer (model photon) (Figure 4a,b) while keeping S grounded and V_G = 5 V. At low frequency (f < 200 Hz), the noise spectrum is mostly following the $1/f^b$ trend ($0 < b < 2$ pink noise), whereas at higher frequencies (f > 200 Hz), it is dominated by instrumental noise, slightly increasing as a function of frequency. Significantly, a local minimum in the noise figure occurs at 518 Hz, i.e., the frequency of the employed mechanical chopper. The contribution of the thermal (Johnson−Nyquist) noise in our system is ∼0.5 × 10^{-15} A/Hz$^{1/2}$ for V_G = 5 V and V_{SD} = 0 V. The bias-dependent NEP (Figure 4d) shows a sequence of minima corresponding to the peaks observed in the responsivity curve. A minimum NEP of 8 pWHz$^{-1/2}$ is reached (Figure 4d). Although it appears still distant from the NEPs of commercially available cooled detectors as hot electron bolometers (NEPs ∼ 10^{-19}−10^{-20} WHz$^{-1/2}$),[15] the envisioned optimization guidelines (see the Supporting Information), combined with the zero dark current and inherent quantum nature, make the proposed technology extremely appealing for quantum-technology-oriented applications.

We then estimate the temporal response of the proposed QD−NW PTE device through the analysis of its transport characteristics. As demonstrated experimentally, the time scales governing the heating/cooling dynamics of the carrier density in InAs NWs fall in the range from 40 fs to 4 ps.[53] These time scales are much faster than the detector rise/fall times, which are limited by its electrical time constant $\tau_{RC} = R_tC_t \sim 1-10$ ns, where R_t (∼1−10 MΩ) and C_t (∼1 fF, includes the bow-tie shunt capacitance, simulated using COMSOL Multiphysics, electrostatic module) are the photodetector resistance and capacitance, respectively.

The achieved performances, combined with the extreme versatility of the QD−NW platform in terms of geometry and chemical composition and with the intrinsically broadband and zero-bias nature of the PTE detection mechanism, unveiled through the choice of the impinging frequency and QD-NW geometry combination, leave room for substantial improvements of the proposed quantum detection concept. For example, we envision that an optimization strategy for the PTE conversion will proceed toward the reduction of the tunnel coupling between the dot and the leads,[31] the engineering of the energy level spacing, and the exploitation of quantum phenomena, e.g., Kondo effect,[54] in search of a balance between detector sensitivity and speed (see the Supporting Information). Therefore, the reported results open a solid perspective for the combination of terahertz technology and few-electron physics to address some of the major challenges of quantum science, as quantum key distribution, quantum communications, and quantum sensing, where sub-shot noise NEPs combined with large quantum efficiencies are required. Furthermore, our work provides a clear understanding of the broadband PTE-driven photoresponse in a QD−NW architecture, offering a framework for disentangling the different physical phenomena that would occur when the impinging photon energy matches the QD level spacing. Finally, the flexibility offered by quantum engineering to optimize device trasport and optical properties, while simultaneously matching the photon energy with the QD energy level spacing, makes our QD InAs/InAsP heterostructured NWs an ideal building block in quantum optics and nanophotonic applications, requiring a precise control of individual photon paths.

■ ASSOCIATED CONTENT

Supporting Information

The Supporting Information is available free of charge at https://pubs.acs.org/doi/10.1021/acs.nanolett.1c02022.

Nanofabrication, electromagnetic simulation of the antenna, constant interaction model, numerical model of transport, evaluation of the photothermoelectric response, optical experiment, and quantum engineering roadmap (PDF)

■ AUTHOR INFORMATION

Corresponding Authors

Leonardo Viti − *National Enterprise for Nanoscience and Nanotechnology (NEST), Consiglio Nazionale delle Ricerche (CNR)−Istituto Nanoscienze and Scuola Normale Superiore, I-56127 Pisa, Italy;* orcid.org/0000-0002-4844-2081; Email: leonardo.viti@nano.cnr.it

Miriam Serena Vitiello − *National Enterprise for Nanoscience and Nanotechnology (NEST), Consiglio Nazionale delle Ricerche (CNR)−Istituto Nanoscienze and Scuola Normale Superiore, I-56127 Pisa, Italy;* orcid.org/0000-0002-4914-0421; Email: miriam.vitiello@sns.it

Authors

Mahdi Asgari − *National Enterprise for Nanoscience and Nanotechnology (NEST), Consiglio Nazionale delle Ricerche (CNR)−Istituto Nanoscienze and Scuola Normale Superiore, I-56127 Pisa, Italy*

Dominique Coquillat − *Laboratoire Charles Coulomb UMR 5221, Centre National de la Recherche Scientifique (CNRS)−Université Montpellier, F-34095 Montpellier, France*

Guido Menichetti − *Graphene Laboratories, Istituto Italiano di Tecnologia, I-16163 Genova, Italy; Dipartimento di Fisica dell'Universit di Pisa, I-56127 Pisa, Italy;* orcid.org/0000-0002-9588-5002

Valentina Zannier − *National Enterprise for Nanoscience and Nanotechnology (NEST), Consiglio Nazionale delle Ricerche (CNR)−Istituto Nanoscienze and Scuola Normale Superiore, I-56127 Pisa, Italy;* orcid.org/0000-0002-9709-5207

Nina Diakonova − *Laboratoire Charles Coulomb UMR 5221, Centre National de la Recherche Scientifique (CNRS)−Université Montpellier, F-34095 Montpellier, France*

Wojciech Knap − *Laboratoire Charles Coulomb UMR 5221, Centre National de la Recherche Scientifique (CNRS)−Université Montpellier, F-34095 Montpellier, France; CENTERA Laboratories, Institute of High Pressure Physics, Polish Academy of Sciences, 01-142 Warsaw, Poland*

Lucia Sorba − *National Enterprise for Nanoscience and Nanotechnology (NEST), Consiglio Nazionale delle Ricerche (CNR)−Istituto Nanoscienze and Scuola Normale Superiore, I-56127 Pisa, Italy;* orcid.org/0000-0001-6242-9417

Complete contact information is available at: https://pubs.acs.org/10.1021/acs.nanolett.1c02022

https://doi.org/10.1021/acs.nanolett.1c02022
Nano Lett. 2021, 21, 8587−8594

Notes

The authors declare no competing financial interest.

■ ACKNOWLEDGMENTS

This work is supported by the European Research Council (ERC) through the ERC Consolidator Grant (681379) SPRINT, the European Union through the Marie Curie H2020-MSCA-ITN-2017, TeraApps (765426), the SUPERTOP Project, QUANTERA ERA-NET Cofound in Quantum Technologies Grant (731473), and the FET-OPEN Project AndQC (828948). Mahdi Asgari, Leonardo Viti, and Miriam Serena Vitiello acknowledge experimental support from Francesco Rossella. Valentina Zannier and Lucia Sorba acknowledge Francesca Rossi for the TEM and EDX analyses. Guido Menichetti thanks Giuseppe Bevilacqua, Alessandro Cresti, and Giuseppe Grosso for useful discussions. Mahdi Asgari and Dominique Coquillat acknowledge experimental support from Cedric Bray. The work is also partially supported by the "International Research Agendas" program of the Foundation for Polish Science (CENTERA MAB/2018/9).

■ REFERENCES

(1) Chatterjee, A.; Stevenson, P.; De Franceschi, S.; Morello, A.; de Leon, N. P.; Kuemmeth, F. Semiconductor Qubits in Practice. *Nat. Rev. Phys.* **2021**, *3* (3), 157−177.
(2) Arakawa, Y.; Holmes, M. J. Progress in Quantum-Dot Single Photon Sources for Quantum Information Technologies: A Broad Spectrum Overview. *Appl. Phys. Rev.* **2020**, *7* (2), 021309.
(3) Sizov, F. Infrared and Terahertz in Application to Biomedicine. *Int. J. Biosens. Bioelectron.* **2018**, *4* (3), 134−136.
(4) Aboud, S. A.; Altemimi, A. B.; Al-Hiiphy, A. R. S.; Yi-Chen, L.; Cacciola, F. A Comprehensive Review on Infrared Heating Applications in Food Processing. *Molecules* **2019**, *24* (22), 4125.
(5) Tonouchi, M. Cutting-Edge Terahertz Technology. *Nat. Photonics* **2007**, *1* (2), 97−105.
(6) Tohmé, L.; Blin, S.; Ducournau, G.; Nouvel, P.; Coquillat, D.; Hisatake, S.; Nagatsuma, T.; Pénarier, A.; Varani, L.; Knap, W.; Lampin, J. F. Terahertz Wireless Communication Using GaAs Transistors as Detectors. *Electron. Lett.* **2014**, *50* (4), 323−325.
(7) Fujiwara, M.; Akiba, M.; Sasaki, M. Study for Far-Infrared and Faint Light Detection Technology. *J. Natl. Inst. Inf. Commun. Technol.* **2004**, *51* (1/2), 51−58.
(8) Karasik, B. S.; Sergeev, A. V.; Prober, D. E. Nanobolometers for THz Photon Detection. *IEEE Trans. Terahertz Sci. Technol.* **2011**, *1* (1), 97−111.
(9) Livache, C.; Martinez, B.; Goubet, N.; Gréboval, C.; Qu, J.; Chu, A.; Royer, S.; Ithurria, S.; Silly, M. G.; Dubertret, B.; Lhuillier, E. A Colloidal Quantum Dot Infrared Photodetector and Its Use for Intraband Detection. *Nat. Commun.* **2019**, *10* (1), 1−10.
(10) Rogalski, A. Quantum Well Photoconductors in Infrared Detector Technology. *J. Appl. Phys.* **2003**, *93* (8), 4355−4391.
(11) Ueda, T.; An, Z.; Hirakawa, K.; Komiyama, S. Charge-Sensitive Infrared Phototransistors: Characterization by an All-Cryogenic Spectrometer. *J. Appl. Phys.* **2008**, *103*, 093109.
(12) Loch, M.; Widenhorn, R.; Bodegom, E. Infrared Response of Charge-Coupled Devices. *Proc. SPIE* **2005**, *5677*, 201.
(13) Nadeev, A. I.; Razenkov, I. A.; Shelefontyuk, D. I.; Shevtsov, E. S. Comparison of an Avalanche Photodiode and a Photomultiplier Tube as Photodetectors of Near-Infrared Radiation in the Photon-Counting Mode. *Instrum. Exp. Tech.* **2018**, *61* (3), 377−381.
(14) Schneider, H.; Maier, T.; Liu, H. C.; Walther, M.; Koidl, P. Ultrasensitive Femtosecond Two-Photon Detector with Resonantly Enhanced Nonlinear Absorption. *Opt. Lett.* **2005**, *30* (3), 287.
(15) Sizov, F. Terahertz Radiation Detectors: The State-of-the-Art. *Semicond. Sci. Technol.* **2018**, *33*, 123001.
(16) Liu, H. C.; Song, C. Y.; SpringThorpe, A. J.; Cao, J. C. Terahertz Quantum-Well Photodetector. *Appl. Phys. Lett.* **2004**, *84* (20), 4068−4070.
(17) Rosencher, A. E.; Fiore, A.; Vinter, B.; Berger, V.; Bois, P.; Nagle, J. *Science* **1996**, *271* (5246), 168−173.
(18) Palaferri, D.; Todorov, Y.; Chen, Y. N.; Madeo, J.; Vasanelli, A.; Li, L. H.; Davies, A. G.; Linfield, E. H.; Sirtori, C. Patch Antenna Terahertz Photodetectors. *Appl. Phys. Lett.* **2015**, *106* (16), 161102.
(19) Jeannin, M.; Bonazzi, T.; Gacemi, D.; Vasanelli, A.; Suffit, S.; Li, L.; Davies, A. G.; Linfield, E.; Sirtori, C.; Todorov, Y. High Temperature Metamaterial Terahertz Quantum Detector. *Appl. Phys. Lett.* **2020**, *117* (25), 251102.
(20) Paulillo, B.; Pirotta, S.; Nong, H.; Crozat, P.; Guilet, S.; Xu, G.; Dhillon, S.; Li, L. H.; Davies, A. G.; Linfield, E. H.; Colombelli, R. Ultrafast Terahertz Detectors Based on Three-Dimensional Meta-Atoms. *Optica* **2017**, *4*, 1451−1456.
(21) Perera, A. G. U.; Ariyawansa, G. Epitaxial Quantum Dot Infrared Photodetectors. In *Wiley Encyclopedia of Electrical and Electronics Engineering*; Webster, J. G., Ed.; John Wiley & Sons, Inc.: Hoboken, NJ, 2014; pp 1−30, DOI: 10.1002/047134608X.W8218.
(22) Gunapala, S. D.; Bandara, S. V.; Rafol, S. B.; Ting, D. Z. Quantum Well Infrared Photodetectors. *Semicond. Semimetals* **2011**, *84*, 59−151.
(23) Phillips, J.; Kamath, K.; Bhattacharya, P. Far-Infrared Photoconductivity in Self-Organized InAs Quantum Dots. *Appl. Phys. Lett.* **1998**, *72* (16), 2020−2022.
(24) Urayama, J.; Norris, T. B.; Singh, J.; Bhattacharya, P. Observation of Phonon Bottleneck in Quantum Dot Electronic Relaxation. *Phys. Rev. Lett.* **2001**, *86* (21), 4930−4933.
(25) Bimberg, D. Quantum Dots: Paradigm Changes in Semiconductor Physics. *Semiconductors* **1999**, *33* (9), 951−955.
(26) Barve, A. V.; Krishna, S. Quantum Dot Infrared Photodetectors. In *Advances in Infrared Photodetectors*; Gunapala, S. D., Rhiger, D. R., Jagadish, C., Eds.; Elsevier, Inc.: Amsterdam, Netherlands, 2011; Semiconductors and Semimetals, Vol. *84*, Chapter 3, pp 153−193, DOI: 10.1016/B978-0-12-381337-4.00003-6.
(27) Kadow, C.; Jackson, A. W.; Gossard, A. C.; Matsuura, S.; Blake, G. A. Self-Assembled ErAs Islands in GaAs for Optical-Heterodyne THz Generation. *Appl. Phys. Lett.* **2000**, *76* (24), 3510−3512.
(28) Kleinschmidt, P.; Giblin, S. P.; Antonov, V.; Hashiba, H.; Kulik, L.; Tzalenchuk, A.; Komiyama, S. A Highly Sensitive Detector for Radiation in the Terahertz Region. *IEEE Trans. Instrum. Meas.* **2007**, *56* (2), 463−467.
(29) Riccardi, E.; Massabeau, S.; Valmorra, F.; Messelot, S.; Rosticher, M.; Tignon, J.; Watanabe, K.; Taniguchi, T.; Delbecq, M.; Dhillon, S.; Ferreira, R.; Balibar, S.; Kontos, T.; Mangeney, J. Ultrasensitive Photoresponse of Graphene Quantum Dots in the Coulomb Blockade Regime to THz Radiation. *Nano Lett.* **2020**, *20*, 5408−5414.
(30) Pogna, E. A. A.; Asgari, M.; Zannier, V.; Sorba, L.; Viti, L.; Vitiello, M. S. Unveiling the Detection Dynamics of Semiconductor Nanowire Photodetectors by Terahertz Near-Field Nanoscopy. *Light: Sci. Appl.* **2020**, *9* (1), 1−12.
(31) Sadre Momtaz, Z.; Servino, S.; Demontis, V.; Zannier, V.; Ercolani, D.; Rossi, F.; Rossella, F.; Sorba, L.; Beltram, F.; Roddaro, S. Orbital Tuning of Tunnel Coupling in InAs/InP Nanowire Quantum Dots. *Nano Lett.* **2020**, *20* (3), 1693−1699.
(32) Romeo, L.; Roddaro, S.; Pitanti, A.; Ercolani, D.; Sorba, L.; Beltram, F. Electrostatic Spin Control in InAs/InP Nanowire Quantum Dots. *Nano Lett.* **2012**, *12* (9), 4490−4494.
(33) Vitiello, M. S.; Coquillat, D.; Viti, L.; Ercolani, D.; Teppe, F.; Pitanti, A.; Beltram, F.; Sorba, L.; Knap, W.; Tredicucci, A. Room-Temperature Terahertz Detectors Based on Semiconductor Nanowire Field-Effect Transistors. *Nano Lett.* **2012**, *12* (1), 96−101.
(34) Viti, L.; Coquillat, D.; Ercolani, D.; Sorba, L.; Knap, W.; Vitiello, M. S. Nanowire Terahertz Detectors with a Resonant Four-Leaf-Clover-Shaped Antenna. *Opt. Express* **2014**, *22* (8), 8996.
(35) Viti, L.; Vitiello, M. S.; Ercolani, D.; Sorba, L.; Tredicucci, A. Se-Doping Dependence of the Transport Properties in CBE-Grown

https://doi.org/10.1021/acs.nanolett.1c02022
Nano Lett. 2021, 21, 8587−8594

InAs Nanowire Field Effect Transistors. *Nanoscale Res. Lett.* **2012**, *7*, 159.
(36) Li, Y.; Qian, F.; Xiang, J.; Lieber, C. M. Nanowire Electronic and Optoelectronic Devices. *Mater. Today* **2006**, *9* (10), 18−27.
(37) Pfund, A.; Shorubalko, I.; Leturcq, R.; Ensslin, K. Top-Gate Defined Double Quantum Dots in InAs Nanowires. *Appl. Phys. Lett.* **2006**, *89*, 252106.
(38) Prete, D.; Erdman, P. A.; Demontis, V.; Zannier, V.; Ercolani, D.; Sorba, L.; Beltram, F.; Rossella, F.; Taddei, F.; Roddaro, S. Thermoelectric Conversion at 30 K in InAs/InP Nanowire Quantum Dots. *Nano Lett.* **2019**, *19* (5), 3033−3039.
(39) Kleinschmidt, P.; Giblin, S.; Tzalenchuk, A.; Hashiba, H.; Antonov, V.; Komiyama, S. Sensitive Detector for a Passive Terahertz Imager. *J. Appl. Phys.* **2006**, *99*, 114504.
(40) Thomas, F. S.; Baumgartner, A.; Gubser, L.; Jünger, C.; Fülöp, G.; Nilsson, M.; Rossi, F.; Zannier, V.; Sorba, L.; Schönenberger, C. Highly Symmetric and Tunable Tunnel Couplings in InAs/InP Nanowire Heterostructure Quantum Dots. *Nanotechnology* **2020**, *31*, 135003.
(41) Zannier, V.; Rossi, F.; Dubrovskii, V. G.; Ercolani, D.; Battiato, S.; Sorba, L. Nanoparticle Stability in Axial InAs−InP Nanowire Heterostructures with Atomically Sharp Interfaces. *Nano Lett.* **2018**, *18* (1), 167−174.
(42) Zannier, V.; Rossi, F.; Ercolani, D.; Sorba, L. Growth Dynamics of InAs/InP Nanowire Heterostructures by Au-Assisted Chemical Beam Epitaxy. *Nanotechnology* **2019**, *30*, 094003.
(43) Persson, A. I.; Björk, M. T.; Jeppesen, S.; Wagner, J. B.; Wallenberg, L. R.; Samuelson, L. $InAs_{1-x}P_x$ Nanowires for Device Engineering. *Nano Lett.* **2006**, *6* (3), 403−407.
(44) Hjort, M.; Lehmann, S.; Knutsson, J.; Zakharov, A. A.; Du, Y. A.; Sakong, S.; Timm, R.; Nylund, G.; Lundgren, E.; Kratzer, P.; Dick, K. A.; Mikkelsen, A. Electronic and Structural Differences between Wurtzite and Zinc Blende Inas Nanowire Surfaces: Experiment and Theory. *ACS Nano* **2014**, *8* (12), 12346−12355.
(45) Liu, D. Design, Fabrication and Chracterization of InAlAs/InGaAs/InAsP Composite Channel HEMTS. Ph.D. Thesis, The Ohio State University, Columbus, OH, 2008.
(46) Kouwenhoven, L. P.; Jauhar, S.; Orenstein, J.; McEuen, P. L.; Nagamune, Y.; Motohisa, J.; Sakaki, H. Observation of Photon-Assisted Tunneling through a Quantum Dot. *Phys. Rev. Lett.* **1994**, *73* (25), 3443−3446.
(47) Hanson, R.; Kouwenhoven, L. P.; Petta, J. R.; Tarucha, S.; Vandersypen, L. M. K. Spins in Few-Electron Quantum Dots. *Rev. Mod. Phys.* **2007**, *79* (4), 1217−1265.
(48) Rinzan, M.; Jenkins, G.; Drew, H. D.; Shafranjuk, S.; Barbara, P. Carbon Nanotube Quantum Dots as Highly Sensitive Terahertz-Cooled Spectrometers. *Nano Lett.* **2012**, *12* (6), 3097−3100.
(49) Bevilacqua, G.; Grosso, G.; Menichetti, G.; Pastori Parravicini, G. Thermoelectric Efficiency of Nanoscale Devices in the Linear Regime. *Phys. Rev. B: Condens. Matter Mater. Phys.* **2016**, *94* (24), 1−14.
(50) Menichetti, G.; Grosso, G.; Parravicini, G. P. Analytic Treatment of the Thermoelectric Properties for Two Coupled Quantum Dots Threaded by Magnetic Fields. *J. Phys. Commun.* **2018**, *2*, 055026.
(51) Riccardi, E.; Massabeau, S.; Valmorra, F.; Messelot, S.; Rosticher, M.; Tignon, J.; Watanabe, K.; Taniguchi, T.; Delbecq, M.; Dhillon, S.; Ferreira, R.; Balibar, S.; Kontos, T.; Mangeney, J. Ultrasensitive Photoresponse of Graphene Quantum Dot in the Coulomb Blockade Regime to THz Radiation. *Nano Lett.* **2020**, *20* (7), 5408−5414.
(52) El Fatimy, A.; Myers-Ward, R. L.; Boyd, A. K.; Daniels, K. M.; Gaskill, D. K.; Barbara, P. Epitaxial Graphene Quantum Dots for High-Performance Terahertz Bolometers. *Nat. Nanotechnol.* **2016**, *11* (4), 335−338.
(53) Eisele, M.; Cocker, T. L.; Huber, M. A.; Plankl, M.; Viti, L.; Ercolani, D.; Sorba, L.; Vitiello, M. S.; Huber, R. Ultrafast Multi-Terahertz Nano-Spectroscopy with Sub-Cycle Temporal Resolution. *Nat. Photonics* **2014**, *8* (11), 841−845.
(54) Dutta, B.; Majidi, D.; García Corral, A.; Erdman, P. A.; Florens, S.; Costi, T. A.; Courtois, H.; Winkelmann, C. B. Direct Probe of the Seebeck Coefficient in a Kondo-Correlated Single-Quantum-Dot Transistor. *Nano Lett.* **2019**, *19* (1), 506−511.

https://doi.org/10.1021/acs.nanolett.1c02022
Nano Lett. 2021, 21, 8587−8594